

Solution Structure of the IIA^{Chitobiose}-IIB^{Chitobiose} complex of the *N,N'*-Diacetylchitobiose Branch of the *Escherichia coli* Phosphotransferase system. *

Young-Sang Jung[†], Mengli Cai[†] and G. Marius Clore[‡]

From the Laboratory of Chemical Physics, NIDDK, National Institutes of Health, Bethesda, Maryland 20892

Running Title: Solution structure of the IIA^{Chb}-IIB^{Chb} complex

[‡]Address correspondence to: G. Marius Clore, Laboratory of Chemical Physics, Bldg 5, Rm. B1-30I, NIDDK, National Institutes of Health, Bethesda, MD 20892-0520. Tel: 301-496-0782; Fax: 301-496-0825; E-mail: mariusc@intra.niddk.nih.gov.

The solution structure of the IIA-IIB complex of the *N,N'*-diacetylchitobiose (Chb) transporter of the *Escherichia coli* phosphotransferase system has been solved by NMR. The active site His-89 of IIA^{Chb} was mutated to Glu to mimic the phosphorylated state and the active site Cys10 of IIB^{Chb} was substituted by serine to prevent intermolecular disulfide bond formation. Binding is weak with a K_D of ~1.3 mM. The two complementary interaction surfaces are largely hydrophobic, with the protruding active site loop (residues 9-16) of IIB^{Chb} buried deep within the active site cleft formed at the interface of two adjacent subunits of the IIA^{Chb} trimer. The central hydrophobic portion of the interface is surrounded by a ring of polar and charged residues that provide a relatively small number of electrostatic intermolecular interactions that serve to correctly align the two proteins. The conformation of the active site loop in unphosphorylated IIB^{Chb} is inconsistent with the formation of a phosphoryl transition state intermediate owing to steric hindrance, especially from the methyl group of Ala12 of IIB^{Chb}. Phosphorylation of IIB^{Chb} is accompanied by a conformational change within the active site loop such that its path from residues 11-13 follows a mirror-like image relative to that in the unphosphorylated state. This involves a transition of the ϕ/ψ angles of Gly13 from the right to left α -helical region, as well as smaller changes in the backbone torsion angles of Ala12 and Met14. The resulting active site conformation is fully compatible with the formation of the His89-P-Cys10 phosphoryl transition state without necessitating any change in relative translation or orientation of the two proteins within the complex.

The bacterial phosphoenolpyruvate:sugar phosphotransferase system (PTS)¹ couples a phosphorylation cascade involving a sequential series of bimolecular protein-protein complexes to active sugar translocation across the membrane and to regulation of an array of cellular processes, including carbon catabolite repression (1-6). The first two steps of the PTS, involving autophosphorylation of enzyme I (EI) by phosphoenolpyruvate and subsequent phosphoryl transfer to the histidine phosphocarrier protein (HPr), are common to all branches of the pathway. The downstream components of the PTS comprise four major classes of sugar specific enzymes II corresponding to the glucose (Glc), mannitol (Mtl), mannose (Man) and lactose/chitobiose (Chb) branches of the PTS. The enzymes II are generally organized into two cytoplasmic domains (IIA and IIB), and one transmembrane domain (IIC), which may or may not be covalently linked to one another. The phosphoryl group is transferred from HPr to IIA, from IIA to IIB and finally from IIB onto the incoming sugar bound to IIC. Despite their similar organization, the IIA and IIB domains of the different sugar-specific branches of the PTS bear no sequence similarity to one another and, with the exception of IIB^{Mtl} (7,8) and IIB^{Chb} (9-11), no structural similarity either. While structures of many of the individual cytoplasmic components of the PTS have been solved either by crystallography (9,12-25) or NMR (7,8,10,11,26-32), the complexes of the PTS have proved refractory to crystallization, presumably because of their weak and transient nature. Weak binding, however, is not an impediment to NMR spectroscopy, and over the last 10 years we have solved the solution structures of the N-terminal domain of enzyme I (EIN) complexed to HPr (33), and the IIA-HPr and IIA-IIB complexes of the glucose, mannitol and mannose branches of the PTS (30,31,34-37). These complexes provide a paradigm

for understanding the structural basis of protein-protein interactions and how individual proteins can recognize multiple, structurally dissimilar, partners.

In the present paper, we present the solution structure of the IIA-IIB complex of the *E. coli* *N,N'*-diacetylchitobiose-specific enzyme II (II^{Chb}), a representative of the lactose/chitobiose branch of the PTS (38-41). The A, B and C domains of II^{Chb} are encoded by a single operon and expressed as three individual proteins. The solution NMR structure of *E. coli* IIA^{Chb} (26) and the crystal structure of the related family member IIA^{Lac} from *Lactobacillus lactis* (21), are symmetric trimers of approximately 35 kDa with three equivalent IIB binding sites. The active site residue, His89, is located deep within a crevice formed by the interface of two helices from adjacent subunits. IIB^{Chb} is a small 11 kDa protein that has been studied by both X-ray crystallography (9) and NMR (10,11), and is structurally similar to IIB^{Mtl} (7,8), despite the absence of any significant sequence similarity. The active site residue, Cys10, of IIB^{Chb} is located within an eight-residue protruding loop (residues 9-16) whose conformation is very similar to that of the low molecular weight protein tyrosine phosphatases (42), including hydrogen bonding interactions in the phosphorylated state between the phosphoryl group and backbone amide protons (11). (Note, throughout the text residues of IIB^{Chb} are shown in italics).

Wild type IIA^{Chb} is highly prone to non-specific aggregation promoted by a disordered thirteen residue N-terminal tail and by metal ions that coordinate three buried aspartic acid residues (Asp92), one from each subunit, at the center of the trimer interface (26). It has previously been shown that aggregation can be completely eliminated by removing the N-terminal tail and mutating Asp92 to Leu to generate a mutant which we refer to hereafter as $\text{IIA}^{\text{Chb*}}$ (26). In the present work, we made use of an active site H89E mutation introduced into $\text{IIA}^{\text{Chb*}}$ to mimic the phosphorylated state. For IIB^{Chb} we introduced a C10S mutation to prevent intermolecular disulfide bridge-mediated dimer formation (9,10). The $\text{IIA}^{\text{Chb*}}$ - IIB^{Chb} complex is transient and weak with an equilibrium dissociation constant (K_D) in the millimolar range. The affinity of $\text{IIA}^{\text{Chb*}}$ (H89E) for IIB^{Chb} (C10S) is a factor of ~1.5 higher than that of $\text{IIA}^{\text{Chb*}}$ (K_D ~1.3 vs ~2 mM) making the phosphomimetic mutant more suitable for NMR structural studies by increasing the population of the complex at the concentrations used in the NMR experiments. The structure of the $\text{IIA}^{\text{Chb*}}$ (H89E)- IIB^{Chb} (C10S) complex reveals the

structural basis of specific recognition and the interactions involved in phosphoryl transfer.

EXPERIMENTAL PROCEDURES

Protein expression and mutagenesis — The genes encoding $\text{IIA}^{\text{Chb*}}$ (corresponding to a NA13/D92L mutant of wild type IIA^{Chb}) and IIB^{Chb} (kindly provided by Dr. Saul Roseman, Johns Hopkins University, Baltimore) were cloned into the pET-11 vector. Additional H89E and C10S mutations of the active site residues of $\text{IIA}^{\text{Chb*}}$ and IIB^{Chb} , respectively were introduced using the QuikChange mutagenesis kit (Stratagene, La Jolla, CA). The H89E mutation in $\text{IIA}^{\text{Chb*}}$ was designed to mimic the charge effects of phosphorylation of His89, and the C10S mutation of IIB^{Chb} was introduced to prevent any potential complications arising from possible intermolecular disulfide bridge formation.

The $\text{IIA}^{\text{Chb*}}$, $\text{IIA}^{\text{Chb*}}$ (H89E), IIB^{Chb} and IIB^{Chb} (C10S) plasmids were introduced into *E. coli* BL21(DE3) (Novagen) cells for protein expression and induced at an A_{600} ~0.8 with 1 mM isopropyl- β -D-thiogalactopyranoside at 37 °C. Cells were grown in either Luria-Bertani medium or minimal medium (in either H₂O or D₂O) with ¹⁵NH₄Cl or ¹⁴NH₄Cl as the main nitrogen source, and U-[¹³C/¹H], U-[¹²C/¹H], U-[¹³C/²H]- or U-[¹²C/²H] glucose as the main carbon source. Because Leu, Val, Ile, Met, Gly, Tyr, and Ser residues are involved in the $\text{IIA}^{\text{Chb*}}$ / IIB^{Chb} interface, selective labeling was also employed in the preparation of NMR samples. For ²H/¹³C/¹⁵N-(Ile/Leu/Val)-methyl-protonated (but otherwise fully deuterated) protein samples, 100 mg of [¹³C₅,3-²H₁] α -ketoisovalerate and 50 mg of [¹³C₄,3,3-²H₂] α -ketobutyrate (Cambridge Isotopes) was added to 1 liter of D₂O medium 1 hour prior to induction (43). ²H/¹²C/¹⁴N-(Ile/Met/Thr-protonated)- $\text{IIA}^{\text{Chb*}}$ (H89E) and ²H/¹²C/¹⁴N-(Gly/Met/Pro/Tyr-protonated)- IIB^{Chb} (C10S) samples were prepared by supplementing 1 liter of D₂O medium with 300 mg of Gly/Ile/Met/Pro/Thr/Tyr (Sigma-Aldrich) at natural isotopic abundance 1 hour prior to induction. After induction (4 and 7 h for growths in H₂O and D₂O, respectively), cells expressing $\text{IIA}^{\text{Chb*}}$ (H89E) or IIB^{Chb} (C10S) were harvested by centrifugation at 15,900 \times g for 25 min.

$\text{IIA}^{\text{Chb*}}$ and $\text{IIA}^{\text{Chb*}}$ (H89E) purification — The cell pellet was re-suspended in 50 ml buffer A (20 mM Tris, pH 8.0, 1mM EDTA, 0.2 mM sodium azide) with 1 mM phenylmethylsulfonyl fluoride (PMSF). The cell suspension was lysed by two passages through a microfluidizer at 15,000 – 23,000 psi and centrifuged at 75,600 \times g for 30 min. The supernatant

was loaded onto a 5 ml HiTrap QFF column (Amersham Biosciences), and IIA^{Chb*} was eluted with a gradient of buffer B (20mM Tris, pH 8.0, 1mM EDTA, 0.2mM sodium azide, 1M NaCl). The eluted protein was subsequently denatured with 4M guanidine-HCl for 15 min. The protein solution was then dialyzed against 2 L of buffer A overnight. After centrifugation of the dialyzed solution to remove precipitated proteins, the supernatant was purified by size exclusion chromatography on a Superdex-75 column (Amersham Biosciences) in buffer C (20 mM Tris, pH 8.0, 1 mM EDTA, 0.2 mM sodium azide, 0.5 M NaCl). The fractions containing IIA^{Chb*} were exchanged into buffer A using an Amicon Ultra-15 (Millipore) filter, loaded onto a mono Q 10/100GL column (Amersham Biosciences), and eluted with a gradient of buffer B.

IIB^{Chb} and IIB^{Chb}(C10S) purification — The cell pellet was re-suspended in 50 ml buffer D (20 mM sodium phosphate, pH 4.5, 0.2mM sodium azide) with 1 mM PMSF. The cell suspension was lysed by two passages through a microfluidizer at 15,000 – 23,000 *psi* and centrifuged at 75,600 × *g* for 30 min. The supernatant was loaded onto a 5 ml HiTrap SP FF column (Amersham Biosciences), and IIB^{Chb}(C10S) was eluted with a gradient of buffer E (20mM sodium phosphate, pH 4.5, 0.2 mM sodium, 1 M NaCl). The eluted protein was further purified by size exclusion chromatography in buffer F (20 mM sodium phosphate, pH 6.5, 0.2 mM sodium azide) on a Superdex-75 column (Amersham Biosciences).

Phosphorylation of IIB^{Chb} — ¹⁵N-labeled IIB^{Chb} was phosphorylated by the addition of 5 μM Enzyme I, 5 μM HPr, 5 μM of IIA^{Chb*}, 5 mM MgCl₂, and 20 mM phosphoenolpyruvate in 20 mM sodium phosphate, pH 6.5, 100 mM NaCl, 0.2 mM sodium azide, and 90% H₂O/ 10% D₂O. Phosphorylation was confirmed by 2D ¹H-¹⁵N correlation spectroscopy which showed large chemical shift perturbations of residues 10-16 comprising the active site loop (11), relative to unphosphorylated IIB^{Chb}. Full length Enzyme I and HPr were expressed and purified as described previously (44).

NMR Data Collection and Analysis — All NMR samples were prepared in a buffer of 20 mM sodium phosphate, pH 6.5, 100 mM NaCl, 0.2 mM sodium azide, and either 90% H₂O/10% D₂O or 99.99% D₂O. IIA^{Chb*} is a symmetric trimer with three equivalent binding sites for IIB^{Chb} (26). To achieve optimal linewidths for NMR spectroscopy, a 1:1 mixture of IIA^{Chb*}(H76E) trimer to IIB^{Chb}(C10S) monomer was employed. NMR spectra were recorded at 20 and 35 °C on Bruker DMX500,

DMX600, DRX600, DRX800, and DRX900 spectrometers equipped with either *x*-, *y*-, and *z*-shielded gradient triple resonance probes or *z*-shielded gradient triple resonance cryoprobes. Spectra were processed with the NMRPipe package (45) and analyzed using the program PIPP (46).

Sequential and sidechain assignments of IIA^{Chb*}(H89E) and IIB^{Chb}(C10S) were derived from the following three-dimensional (3D) double and triple resonance through-bond correlation experiments (47-49): HNCA, HN(CO)CA, HNCACB, CBCA(CO)HN, HAHN, HNCA-TROSY, HN(CO)CA-TROSY, HNCB-TROSY, HN(CO)CB-TROSY, C(CCO)NH, H(CCO)NH, and HCCH-TOCSY. 3D ¹⁵N-separated, ¹³C-separated and ¹³C/¹³C separated nuclear Overhauser enhancement (NOE) experiments were used to facilitate sidechain assignments (47,48).

Backbone ¹D_{NH} residual dipolar couplings (RDC) were obtained from the difference in ¹J_{HN} scalar couplings measured in dilute liquid crystalline medium (phage pf1 (50,51)) and isotropic (water) media, measured using two-dimensional in-phase/anti-phase (IPAP) ¹H-¹⁵N heteronuclear single quantum coherence (HSQC) spectra (52).

Intermolecular NOEs were observed on the IIA^{Chb*}(H89E)-IIB^{Chb}(C10S) complex in D₂O buffer using 3D ¹²C-filtered(F₁)/¹³C-separated(F₂) or ¹³C-separated(F₂)/¹²C-filtered(F₃) NOE experiments, and in H₂O buffer using 2D ¹⁵N-separated/¹³C-edited and ¹³C-separated/¹⁵N-edited NOE experiments (53,54). Nine different combinations of isotope-labeled complexes were used for analysis of intermolecular NOEs (Table 1).

Structure Calculations — NOE-derived inter-proton distance restraints were classified into loose approximate distance ranges of 1.8–2.7, 1.8–3.5, 1.8–5.0, and 1.8–6.0 Å corresponding to strong, medium, weak, and very weak NOE cross-peak intensities, respectively (55); an empirical correction of 0.5 Å was added to the upper distance bounds of distance restraints involving methyl groups to account for the higher apparent intensity of methyl resonances (56). NOEs involving non-stereospecifically assigned methyl, methylene, and aromatic protons were represented by a (Σ*r*⁻⁶)^{-1/6} sum (57). Backbone torsion angle restraints for the active site loop of IIB^{Chb}(C10S) and phospho-IIB^{Chb}, and for the mobile loop (residues 75-84) of IIA^{Chb*}(H89E) were derived from chemical shifts using the program TALOS+ (58).

Structures were calculated using conjoined rigid body/torsion angle-simulated annealing (59) with the program Xplor-NIH (60,61). The minimized target

function comprises NOE-derived interproton distance restraints, torsion angle restraints, RDC restraints (62), $^{13}\text{C}\alpha/^{13}\text{C}\beta$ chemical shift restraints (63), a quartic van der Waals repulsion term for the non-bonded contacts (64), a multidimensional torsion angle database potential of mean force (65), and a gyration volume potential to ensure optimal packing (66).

Structure figures were generated using the programs VMD-XPLOR (67) and GRASP (68). Reweighted atomic probability density maps were calculated as described previously (69).

RESULTS AND DISCUSSION

Equilibrium binding of IIA^{Chb}(H89E) and IIB^{Chb}(C10S)* — The binding of IIA^{Chb*} and the active site IIA^{Chb*}(H89E) phosphomimetic mutant (at natural isotopic abundance) to U- ^{15}N -labeled IIB^{Chb}(C10S) was monitored by ^1H - ^{15}N correlation spectroscopy. Exchange between the complex and free proteins is fast on the chemical shift time scale. The pattern of $^1\text{H}_\text{N}/^{15}\text{N}$ chemical shift perturbations observed for the binding of IIA^{Chb*} and IIA^{Chb*}(H89E) to IIB^{Chb}(C10S) is very similar but the magnitude of the perturbations is smaller for IIA^{Chb*} than IIA^{Chb*}(H89E). This is due to the fact that the binding of IIA^{Chb*} to IIB^{Chb}(C10S) is weaker ($K_D \sim 2.1 \pm 0.5$ mM) than that of IIA^{Chb*}(H89E) ($K_D \sim 1.3 \pm 0.3$ mM; cf. Fig. 1), and hence the fraction of complex formed under the same experimental conditions (protein concentrations ≤ 1 mM) is considerably reduced. For this reason, all structural studies were conducted with the IIA^{Chb*}(H89E) phosphomimetic mutant.

Structural studies were carried out on samples comprising 1 mM IIA^{Chb*}(H89E) trimer and 1 mM IIB^{Chb}(C10S). Under these conditions 51.6% of IIA^{Chb*}(H89E) and 64.4% of IIB^{Chb}(C10S) are in the bound state. Since IIA^{Chb*} is a symmetric trimer with 3 equivalent binding sites for IIB^{Chb}, one can calculate that the percentage of IIA^{Chb*}(H89E) with one, two and three IIB^{Chb}(C10S) molecules bound is 39.7, 10.9 and 1.0%, respectively; the corresponding percentages, expressed in terms of IIB^{Chb}(C10S) are 39.7, 21.7 and 3.0%, respectively. Given molecular weights of 33.6 kDa and 11.4 kDa for free IIA^{Chb*}(H89E) and IIB^{Chb}(C10S), respectively, and the fact that all species are in fast exchange with one another, the linewidths of IIA^{Chb*}(H89E) and IIB^{Chb}(C10S) in the NMR sample are determined by population weighted average molecular weights of 41.0 and 36.2 kDa, respectively.

Structure determination — Since the chemical shift perturbations observed upon complex formation are small, one can conclude that there are no significant backbone structural changes (within the limits of the NMR method) induced within either IIA^{Chb*}(H89E) or IIB^{Chb}(C10S). We therefore proceeded to solve the structure of the complex using conjoined rigid body/torsion angle dynamics simulated annealing (59,70), largely on the basis of intermolecular NOE data. In this approach, the backbone (except for certain selected regions, see below) and non-interfacial sidechain coordinates are treated as rigid bodies with rotational and translational degrees of freedom, while the interfacial sidechains are given full torsional degrees of freedom.

The chemical shift differences between IIA^{Chb*} and IIA^{Chb*}(H89E) are limited to the immediate vicinity of the mutation, and $^1\text{D}_{\text{NH}}$ residual dipolar coupling (RDC) measurements on free IIA^{Chb*}(H89E) indicate excellent agreement between observed RDCs for helical residues and those calculated from the NMR structure (restrained regularized mean coordinates) of IIA^{Chb*} (26). The RDC *R*-factor is 8.7% (defined as $\{< (D_{\text{obs}} - D_{\text{calc}})^2 > / 2 < D_{\text{obs}}^2 > \}^{1/2}$ (71), where D_{obs} are the observed RDCs, and D_{calc} are the calculated RDCs obtained by singular value decomposition against the coordinates of the protein (72)). The alignment tensor of IIA^{Chb*}(H89E) is axially symmetric, as expected for a symmetric trimer, with a magnitude of -11.3 Hz for the axial component (D_a^{NH}). We therefore used the NMR structure of IIA^{Chb*} in the conjoined rigid body/torsion angle dynamics simulated annealing calculations. However, since the loop connecting helices 2 and 3 is partially disordered (i.e. highly mobile) in solution and contributes to the interface with IIB^{Chb}, the backbone of residues 75-84 was also give torsional degrees of freedom.

IIB^{Chb}(C10S) strongly interacts with the alignment medium (phage pf1) in the absence of salt; RDC measurements were therefore carried out in 100 and 400 mM NaCl using 10 and 17 mg/ml phage pf1, yielding values of 25.5 and -8.5 Hz for D_a^{NH} , respectively, and a rhombicity η of ~ 0.4 . The RDC *R*-factors are summarized in Table 2 and allow one to conclude the following: (a) both the 1.8 Å resolution X-ray structure of IIB^{Chb}(C10S) (9) and the NMR structure of phospho-IIB^{Chb} (11) provide a much better representation of the actual solution structure of IIB^{Chb}(C10S) than does the NMR structure of IIB^{Chb}(C10S) (10), reflecting the lower coordinate accuracy of the latter; (b) there are very large discrepancies between observed and calculated

RDCs within the active site loop (residues 9-16) for both the X-ray structure of IIB^{Chb}(C10S) and the NMR structure of phospho-IIB^{Chb}, reflected in very high RDC R-factors for this region; (c) removing the RDCs for the active site residues results in excellent agreement between observed and calculated RDCs with lower RDC R-factors for the X-ray structure of IIB^{Chb}(C10S). Therefore, the coordinates of the X-ray structure of IIB^{Chb}(C10S) (9) were used in the calculations, with the backbone of the active site loop (residues 9-16), given torsion degrees of freedom. The observed RDC R-factors of 8-9% observed for the X-ray structure of IIB^{Chb}(C10S), excluding the active site loop, are as expected for a crystal structure solved at 1.5 to 2 Å resolution (73,74). It is worth noting that phosphorylation of IIB^{Chb} is accompanied by a large conformational change within the active site loop as manifested both by RDCs (Table 2) and by significant differences in backbone (N, Cα, Hα, and Cβ) chemical shifts (11). Excluding the active site loop, the crystal structure of IIB^{Chb}(C10S) still displays lower RDC R-factors than the NMR structure of phospho-IIB^{Chb} (Table 2). However, the RDCs within the active site loop are now in excellent agreement with the NMR structure of phospho-IIB^{Chb} but exhibit very large discrepancies with respect to the X-ray structure of IIB^{Chb}(C10S) (Table 2).

The intermolecular NOE data were derived from a large series of isotope-filtered/isotope-separated intermolecular NOE experiments (53). Because of the relatively large size of the complex and extensive chemical shift overlap, nine different labeling combinations (Table 1), including amino acid specific labeling, were used to eliminate any ambiguities in intermolecular NOE assignments. Examples of the quality of the intermolecular NOE data are shown in Fig. 2.

In protein-protein complexes of the PTS that we have solved previously (30,31,33-37), it is usually possible to derive sidechain torsion angle restraints for interfacial sidechains based on heteronuclear ³J scalar couplings and short mixing time NOE data (53). In this instance, the complex is not fully saturated owing to weak binding (*K_D* ~ 1.3 mM) and there is a significant proportion of each component in the free state. We therefore employed a heuristic approach in which the interfacial sidechains were given torsional degrees of freedom but restrained within the χ₁ and, where appropriate, χ₂ rotamers occupied in the free structures, unless these were inconsistent with the intermolecular NOE data.

Unfortunately we were not able to use RDC data to provide information on the relative orientation of the

two components within the complex. In a simple case of a weak binding binary complex in fast exchange on the chemical shift scale, the observed RDCs are weighted averages of the RDCs in the free and bound state, so that it is possible in principle to back-calculate the RDCs for the pure complex providing one knows exactly the fraction of the bound species (35,75). However, for the IIA^{Chb*}(H89E)-IIB^{Chb}(C10S) complex, the bound species comprises a mixture of three states with one, two and three IIB^{Chb}(C10S) molecules bound to the IIA^{Chb*}(H89E) trimer, each with its own alignment tensor. Deconvolution of the alignment tensors for the individual bound states is not feasible, thereby precluding the use of RDCs in this system. Moreover, the alignment media that we explored (pf1, strained gels and PEG/hexanol (72)) all displayed differential interaction with one of the partners, making any extrapolation of average RDCs for the bound states unreliable.

A summary of the structural statistics is given in Table 3, and a best-fit superposition of the final 90 simulated annealing structures is shown in Fig. 3A. The NOE-derived interproton distance restraints comprised 40 intermolecular NOEs (per bound IIB^{Chb} molecule), as well as intramolecular NOEs related to those portions of the IIB^{Chb}(C10S) backbone that were given torsional degrees of freedom. The agreement of the RDCs within the active site loop of IIB^{Chb}(C10S) is comparable to that of the rest of the protein (Table 4). The relative orientation of IIB^{Chb}(C10S) to IIA^{Chb*}(H89E) is well defined with a precision of 0.3±0.1 Å for the backbone of the complete complex (IIA^{Chb*} and IIB^{Chb} best-fitted overall), 0.9±0.3 Å for the backbone of IIB^{Chb} with best-fitting to IIA^{Chb*}, and 1.2±0.4 Å for IIA^{Chb*} with best-fitting to IIB^{Chb}. The coordinate precision for the interfacial sidechains is 0.9±0.1 Å.

Overall structure of the IIA^{Chb}(H89E)-IIB^{Chb}(C10S) complex* — The overall structure of the complex is shown in Fig. 3 with one, two and three molecules of IIB^{Chb}(C10S) bound.

IIA^{Chb*} is a symmetric trimer (26). Each subunit comprises a three-helix bundle (α1, residues 14-44; α2, residues 46-74, α3, residues 84-114) in an up-down topology with α2 antiparallel to α1 and α3. The trimer interface consists of a parallel coiled-coil formed by helix α3 of each subunit. The active site residue, His89, is located in helix α3 and lies in a deep groove bounded by helix α1 of its own subunit and helices α2 and α3 of an adjacent subunit. In the representations shown in this paper with subunits A, B and C of IIA^{Chb*} colored in blue, gold and green,

respectively, there are three identical binding sites for IIB^{Chb}, located at the interface of subunits A and C, subunits C and B, and subunits B and A, with the first named subunit of each binding site bearing the active site His89 (Figs. 3B and C).

IIB^{Chb} is a mixed α/β protein comprising 5 helices (residues 12-30, 43-49, 63-71, 80-86 and 88-105), and 4 β -strands (residues 4-9, 34-39, 53-56 and 76-78) arranged in a -1x, 2x, 1x topology (9-11). The active site residue, Cys10, is located in an exposed active site loop (residues 9-16) that forms a protrusion on the surface of the protein. The overall topology of IIB^{Chb} is similar to that of IIA^{Mtl} (7) although the percentage sequence identity is only 8%. In the NMR structure of phospho-IIB^{Chb} (11) but not the X-ray structure of IIB^{Chb}(C10S) (9), the active site loop has a conformation that is similar to that of IIB^{Mtl} (both unphosphorylated (7) and phosphorylated (8)) and the low molecular weight protein tyrosine phosphatases (42), except that the residues located at *i*+1 and *i*+2 of the active site cysteine are replaced by only a single residue in IIB^{Chb}.

Since the three IIB^{Chb} binding sites on IIA^{Chb*} are identical, we will simply consider the interaction of IIB^{Chb}(C10S) with the A and C subunits of IIA^{Chb*}(H89E), where the contributing active site histidine (His89) originates from the A subunit (Figs. 3A, 4 and 5). A total of 1836 Å² is buried upon complexation, 927 Å² originating from IIA^{Chb*}(H89E) and 909 from IIB^{Chb}(C10S). The interface accessible surface area contributed by the A and C subunits of IIA^{Chb*}(H89E) is approximately equal. The interface comprises 15 residues each from the A and C subunits of IIA^{Chb*}(H89E) and 29 residues from IIB^{Chb}(C10S); 4 residues of the latter interact simultaneously with the A and C subunits of IIA^{Chb*}(H89E) (Fig. 4C). The interface is ellipsoidal in shape with an eccentricity of ~0.3 (where values of 0 and 1 indicate a perfect circle and a straight line, respectively), the gap volume index (ratio of gap volume to interface accessible surface area) is 3.3 Å, and the rms deviation of the interface atoms from a least-squares plane through these atoms is 3.7 Å (concave; Fig. 5, left panel) for IIA^{Chb*}(H89E) and 3.3 Å (convex; Fig. 5, right panel) for IIB^{Chb}(C10S). These values are typical of transient complexes (76,77).

Stereoviews depicting details of the interface are shown in Figs. 4A and B, and a summary of the intermolecular contacts is provided in Fig. 4C. The active site loop, a 3¹⁰ helix (residues 58-62) and helix α 4 of IIB^{Chb}(C10S) are in contact with helices α 1 and α 3 of the A subunit of IIA^{Chb*}(H89E) (Fig. 4A).

Helices α 1 and α 2, the C-terminal end of strand β 2 and the subsequent 3¹⁰ helix (residues 40-42) of IIB^{Chb}(C10S) contact helices α 2 and α 3 of the C subunit of IIA^{Chb*}(H89E), as well as some residues in the disordered loop connecting these two helices in IIA^{Chb*}(H89E) (Fig. 4B). The intermolecular interactions are largely hydrophobic with 50-60% of the interfacial residues being non-polar. Met14 of the active site loop of IIB^{Chb}(C10S) is involved in a very large number of intermolecular hydrophobic interactions with methyl group clusters of Val and Leu residues, specifically Val21^A and Val86^A of the A subunit and Val83^C, Leu87^C and Val88^C of the C subunit of IIA^{Chb*}(H89E). Two other methionine residues, Met22^A and Met81^C of IIA^{Chb*}(H89E) are also involved in an array of intermolecular hydrophobic interactions, with C10S, Pro58, Gln59 and Tyr84, and with Leu18, Lys22 and Val87, respectively, of IIB^{Chb}(C10S). There are only two intermolecular salt bridge/hydrogen bonding interactions: between Arg24 and Glu73^C, and between Ser17 and the backbone carbonyl of Ile72^C (Fig. 4B). These are supplemented by 7 longer-range electrostatic interactions, 5 involving the A chain and 2 the B chain of IIA^{Chb*}(H89E) (Fig. 4C). Of these, two involve interactions between charged sidechains (E15^A and Lys86, and K70^C and E37). The remainder involve interactions either between polar groups or between polar and charged groups. An example of the former would include the interaction between the sulfur atom of Met22^A and the hydroxyl group of Tyr84 (Fig. 4A). An example of the latter is the interaction between the carboxylate of Glu19^A and the hydroxyl group of Ser81 and the amide group of Gln59 (Fig. 4A).

As in previously solved complexes of the PTS (30,31,33-37), the center of each interface is largely hydrophobic, surrounded by a ring of polar and charged residues (Fig. 5). Of note is that the interaction surface of IIB^{Chb} contains both positively and negatively charged residues, similar to IIB^{Glc} (31), IIB^{Mtl} (36) and IIB^{Man} (35), but in contrast to HPr (33,34,37) where the charged residues on the interaction surface are entirely positive. This ensures that the IIB domains interact with their corresponding IIA domains, but not with enzyme I, despite the fact that the binding site on all the sugar-specific enzymes IIA is common to both HPr and IIB, and HPr uses the same binding surface to interact with both enzymes IIA and EI.

The active site and the phosphoryl transition state

The conformation of the active site loop (residues 9-16) of IIB^{Chb}(C10S) in the complex is not compatible with the formation of a pentacoordinate

phosphoryl transition state in which the phosphorus atom lies in the plane of the imidazole ring of His89^A and the P-Sγ-Cβ bond angle of Cys10 lies between 90 and 130°. This is because the location of Ala12 sterically occludes the formation of a phosphoryl transition state (Fig. 6A). The same is true of the X-ray structure of IIB^{Chb}(C10S) (9). Although there is a small displacement (1.3 Å) of the backbone of the active site loop of IIB^{Chb}(C10S) between the current structure (based on RDCs within the active site loop) and the crystal structure, the conformation of the loop in the two structures is actually very similar and the differences in backbone torsion angles are relatively small. In the conformation of the active site loop of phospho-IIB^{Chb} (11), however, the path of the polypeptide chain from residues 11-13 follows a mirror-like image relative to the unphosphorylated active site loop.

To model the transition state, therefore, we kept the coordinates of IIA^{Chb*} and IIB^{Chb} within the complex fixed, with the exception of the backbone of the active site loop (residues 9-16) of IIB^{Chb}, the backbone immediately adjacent to the active site histidine (residues 87-91 of subunit A) of IIA^{Chb*}, and the interfacial sidechains in close proximity to Cys10 and His89^A, which were given torsional degrees of freedom and subjected to simulated annealing refinement on the basis of the experimental intermolecular NOE restraints and the RDCs collected on free phospho-IIB^{Chb}. In addition, restraints were included to define the geometry of the phosphoryl group relative to Cys10 and His89^A in the transition state, as described for the phosphoryl transition state of the IIA^{Mtl}-IIB^{Mtl} complex (36). The results are shown in Figs. 6A and B. The active site loop of IIB^{Chb} in the transition state adopts a very similar conformation to that seen in the previously determined NMR structure of phospho-IIB^{Chb} (11) with a backbone rms difference of 0.8 Å, and the RDCs within the active site loop are well satisfied (Table 5). The key conformational changes within the active site loop of IIB^{Chb} are the transition of the φ/ψ angles of Gly13 from the right (~ -60°/-40°) to left α-helical region (~100°/30°) of the Ramachandran plot, a shift in the φ/ψ angles of Met14 away from the α-helical region (from ~ -50°/-50° to ~ -110°/-70°), and a shift of the φ/ψ angles of Ala12 from the β region (~ -150°/70°) to the helical region (~ -110°/-25°). The changes in the backbone of residues 87^A-91^A of IIA^{Chb*} are minimal with atomic rms displacements of less than 0.6 Å (Fig. 6A). It can be readily seen that as a consequence of the conformational change in the active site loop of IIB^{Chb}, Ala12 no longer occludes

the phosphoryl group and the path followed by the backbone readily permits the formation of a phosphoryl transition state His89-P-Cys10 intermediate.

Although the structure of phospho-IIA^{Chb*} has not been solved, the phosphorylated state is easily modeled from the structure of unphosphorylated IIA^{Chb*} (26): minimal changes in the χ₁ and χ₂ angles of His89^A are all that are required to permit the formation of hydrogen bonds from the sidechain amide of Gln91^C and the Ne2-H proton of His93^A to the phosphoryl group. In the transition state these distances are lengthened but bridging hydrogen bonds involving water molecules could clearly be formed (Fig. 6C). The phosphoryl group in the transition state is stabilized by an array of hydrogen bonds from the IIB^{Chb} active site loop, including the backbone amides of Ala12, Met 14 and Ser15, and the hydroxyl groups of Ser11 and Ser15; in addition, hydrogen bonds from the backbone amides of Ser11 and Gly13 to the sulfur atom to Cys10 further stabilize the conformation (Figs. 6B,C). Many of these interactions are maintained upon shortening of the S-P bond to form phospho-IIB^{Chb} (11). The interactions stabilizing the phosphoryl group in both the IIA^{Chb*}-P-IIB^{Chb} transition state and phospho-IIB^{Chb} (11) are very similar to those observed in phospho-IIB^{Mtl} (8) and the phosphorylated state of the low molecular weight protein tyrosine phosphatases (42). Presumably, the reason that the active site loop of IIB^{Chb} undergoes a conformational change upon phosphorylation whereas that of IIB^{Mtl} does not, resides in the fact that the single residue deletion within the active site loop of IIB^{Chb}, relative to IIB^{Mtl}, results in stereochemical strain that can only be overcome by numerous interactions between the protein backbone and the phosphoryl group.

Further examination of the IIA^{Chb*}-P-IIB^{Chb} transition state reveals that the phosphoryl group is buried within a largely hydrophobic environment provided by Ala12 and Met14 of IIB^{Chb} and Val21^A, Met22^A, Ile25^A, Ile72^C and Leu87^C of IIA^{Chb*}. This configuration is common to all protein-protein complexes of the PTS solved to date (30,31,33-37), including the EIN-HP_r complex that is common to all branches of the pathway, as well as the complexes involving sugar-specific components.

Concluding Remarks — We have determined the solution structure of the IIA^{Chb*}(H89E)-IIB^{Chb}(C10S) complex, and shown that this structure is fully compatible with the formation of a phosphoryl transition state when the active site loop of IIB^{Chb} adopts the conformation found in phosphorylated

IIB^{Chb}. As previously noted, the overall topology of IIB^{Chb} and IIB^{Mtl} are remarkably similar, despite 8% sequence identity, and the C α atoms of 71 out of 106 residues can be superimposed with an atomic rms difference of 2 Å. Fig. 7 shows a comparison of the phosphoryl transition states of the two complexes with the coordinates of IIB^{Chb} and IIB^{Mtl} superimposed. The structures of the IIA^{Chb*} trimer and IIA^{Mtl} monomer bear no resemblance to one another, and with the exception of a single turn of helix that fortuitously overlaps, the structural elements making up the binding site are entirely different. Nevertheless, the position of the His-P-Cys phosphoryl transition state is remarkably similar. In addition, the distribution of hydrophobic, polar and charged residues within the binding sites of IIA^{Chb*} and IIA^{Mtl}, and likewise IIB^{Chb} and IIB^{Mtl}, is broadly

similar (cf. compare Fig. 5 of this paper with Fig. 6 of (36)), although the interaction of IIA^{Chb*} with IIB^{Chb} involves a somewhat larger preponderance of hydrophobic residues than that between IIA^{Mtl} and IIB^{Mtl}, and the cleft in which the active site histidine of IIA^{Chb*} is located is both deeper and narrower than that for IIA^{Mtl}. Thus, one might argue that these two PTS complexes from distinct sugar branches of the pathway illustrate an example of convergent evolution of the surfaces of active sites (in terms of shape and distribution of residue type) generated by completely different underlying backbone structural elements.

Acknowledgments — We thank Dan Garrett for software support, and Chun Tang for many helpful discussions.

REFERENCES

1. Deutscher, J., Francke, C., and Postma, P. W. (2006) *Microbiol. Mol. Biol. Rev.* **70**, 939-1031
2. Kundig, W., Ghosh, S., and Roseman, S. (1964) *Proc. Natl. Acad. Sci. U. S. A.* **52**, 1067-1074
3. Meadow, N. D., Fox, D. K., and Roseman, S. (1990) *Annu. Rev. Biochem.* **59**, 497-542
4. Postma, P. W., Lengeler, J. W., and Jacobson, G. R. (1993) *Microbiol. Rev.* **57**, 543-594
5. Robillard, G. T., and Broos, J. (1999) *Biochim. Biophys. Acta* **1422**, 73-104
6. Siebold, C., Flukiger, K., Beutler, R., and Erni, B. (2001) *FEBS Lett.* **504**, 104-111
7. Legler, P. M., Cai, M., Peterkofsky, A., and Clore, G. M. (2004) *J. Biol. Chem.* **279**, 39115-39121
8. Suh, J. Y., Tang, C., Cai, M., and Clore, G. M. (2005) *J. Mol. Biol.* **353**, 1129-1136
9. van Montfort, R. L., Pijning, T., Kalk, K. H., Reizer, J., Saier, M. H., Jr., Thunnissen, M. M., Robillard, G. T., and Dijkstra, B. W. (1997) *Structure* **5**, 217-225
10. Ab, E., Schuurman-Wolters, G., Reizer, J., Saier, M. H., Dijkstra, K., Scheek, R. M., and Robillard, G. T. (1997) *Protein Sci.* **6**, 304-314
11. Ab, E., Schuurman-Wolters, G. K., Nijlant, D., Dijkstra, K., Saier, M. H., Robillard, G. T., and Scheek, R. M. (2001) *J. Mol. Biol.* **308**, 993-1009
12. Teplyakov, A., Lim, K., Zhu, P. P., Kapadia, G., Chen, C. C., Schwartz, J., Howard, A., Reddy, P. T., Peterkofsky, A., and Herzberg, O. (2006) *Proc. Natl. Acad. Sci. U. S. A.* **103**, 16218-16223
13. Oberholzer, A. E., Bumann, M., Schneider, P., Bachler, C., Siebold, C., Baumann, U., and Erni, B. (2005) *J. Mol. Biol.* **346**, 521-532
14. Oberholzer, A. E., Schneider, P., Siebold, C., Baumann, U., and Erni, B. (2009) *J. Biol. Chem.*
15. Liao, D. I., Silverton, E., Seok, Y. J., Lee, B. R., Peterkofsky, A., and Davies, D. R. (1996) *Structure* **4**, 861-872
16. Marquez, J., Reinelt, S., Koch, B., Engelmann, R., Hengstenberg, W., and Scheffzek, K. (2006) *J. Biol. Chem.* **281**, 32508-32515
17. Herzberg, O., Reddy, P., Sutrina, S., Saier, M. H., Jr., Reizer, J., and Kapadia, G. (1992) *Proc. Natl. Acad. Sci. U. S. A.* **89**, 2499-2503
18. Jia, Z., Quail, J. W., Waygood, E. B., and Delbaere, L. T. (1993) *J. Biol. Chem.* **268**, 22490-22501
19. Liao, D. I., Kapadia, G., Reddy, P., Saier, M. H., Jr., Reizer, J., and Herzberg, O. (1991) *Biochemistry* **30**, 9583-9594
20. Worthylake, D., Meadow, N. D., Roseman, S., Liao, D. I., Herzberg, O., and Remington, S. J. (1991) *Proc. Natl. Acad. Sci. U. S. A.* **88**, 10382-10386
21. Sliz, P., Engelmann, R., Hengstenberg, W., and Pai, E. F. (1997) *Structure* **5**, 775-788
22. Nunn, R. S., Markovic-Housley, Z., Genovesio-Taverne, J. C., Flukiger, K., Rizkallah, P. J., Jansonius, J. N., Schirmer, T., and Erni, B. (1996) *J. Mol. Biol.* **259**, 502-511
23. Schauder, S., Nunn, R. S., Lanz, R., Erni, B., and Schirmer, T. (1998) *J. Mol. Biol.* **276**, 591-602

24. van Montfort, R. L., Pijning, T., Kalk, K. H., Hangyi, I., Kouwijzer, M. L., Robillard, G. T., and Dijkstra, B. W. (1998) *Structure* **6**, 377-388
25. Orriss, G. L., Erni, B., and Schirmer, T. (2003) *J. Mol. Biol.* **327**, 1111-1119
26. Tang, C., Williams, D. C., Jr., Ghirlando, R., and Clore, G. M. (2005) *J. Biol. Chem.* **280**, 11770-11780
27. Kalbitzer, H. R., and Hengstenberg, W. (1993) *Eur. J. Biochem.* **216**, 205-214
28. Wittekind, M., Rajagopal, P., Branchini, B. R., Reizer, J., Saier, M. H., Jr., and Klevit, R. E. (1992) *Protein Sci.* **1**, 1363-1376
29. Eberstadt, M., Grdadolnik, S. G., Gemmecker, G., Kessler, H., Buhr, A., and Erni, B. (1996) *Biochemistry* **35**, 11286-11292
30. Hu, J., Hu, K., Williams, D. C., Jr., Komlos, M. E., Cai, M., and Clore, G. M. (2008) *J. Biol. Chem.* **283**, 11024-11037
31. Cai, M., Williams, D. C., Jr., Wang, G., Lee, B. R., Peterkofsky, A., and Clore, G. M. (2003) *J. Biol. Chem.* **278**, 25191-25206
32. Garrett, D. S., Seok, Y. J., Liao, D. I., Peterkofsky, A., Gronenborn, A. M., and Clore, G. M. (1997) *Biochemistry* **36**, 2517-2530
33. Garrett, D. S., Seok, Y. J., Peterkofsky, A., Gronenborn, A. M., and Clore, G. M. (1999) *Nature Struct. Biol.* **6**, 166-173
34. Cornilescu, G., Lee, B. R., Cornilescu, C. C., Wang, G., Peterkofsky, A., and Clore, G. M. (2002) *J. Biol. Chem.* **277**, 42289-42298
35. Williams, D. C., Jr., Cai, M., Suh, J. Y., Peterkofsky, A., and Clore, G. M. (2005) *J. Biol. Chem.* **280**, 20775-20784
36. Suh, J. Y., Cai, M., Williams, D. C., Jr., and Clore, G. M. (2006) *J. Biol. Chem.* **281**, 8939-8949
37. Wang, G., Louis, J. M., Sondej, M., Seok, Y. J., Peterkofsky, A., and Clore, G. M. (2000) *EMBO J.* **19**, 5635-5649
38. Keyhani, N. O., Wang, L. X., Lee, Y. C., and Roseman, S. (2000) *J. Biol. Chem.* **275**, 33084-33090
39. Keyhani, N. O., Bacia, K., and Roseman, S. (2000) *J. Biol. Chem.* **275**, 33102-33109
40. Keyhani, N. O., Boudker, O., and Roseman, S. (2000) *J. Biol. Chem.* **275**, 33091-33101
41. Keyhani, N. O., and Roseman, S. (1997) *Proc. Natl. Acad. Sci. U. S. A.* **94**, 14367-14371
42. Zhang, M., Van Etten, R. L., and Stauffacher, C. V. (1994) *Biochemistry* **33**, 11097-11105
43. Goto, N. K., Gardner, K. H., Mueller, G. A., Willis, R. C., and Kay, L. E. (1999) *J. Biomol. NMR* **13**, 369-374
44. Suh, J. Y., Cai, M., and Clore, G. M. (2008) *J. Biol. Chem.* **283**, 18980-18989
45. Delaglio, F., Grzesiek, S., Vuister, G. W., Zhu, G., Pfeifer, J., and Bax, A. (1995) *J. Biomol. NMR* **6**, 277-293
46. Garrett, D. S., Powers, R., Gronenborn, A. M., and Clore, G. M. (1991) *J. Magn. Reson.* **95**, 214-220
47. Clore, G. M., and Gronenborn, A. M. (1991) *Science* **252**, 1390-1399
48. Bax, A., and Grzesiek, S. (1993) *Acc. Chem. Res.* **26**, 131-138
49. Yang, D. W., and Kay, L. E. (1999) *J. Biomol. NMR* **13**, 3-10
50. Clore, G. M., Starich, M. R., and Gronenborn, A. M. (1998) *J. Am. Chem. Soc.* **120**, 10571-10572
51. Hansen, M. R., Mueller, L., and Pardi, A. (1998) *Nature Struct. Biol.* **5**, 1065-1074
52. Ottiger, M., Delaglio, F., and Bax, A. (1998) *J. Magn. Reson.* **131**, 373-378
53. Clore, G. M., and Gronenborn, A. M. (1998) *Trends Biotechnol.* **16**, 22-34
54. Cai, M., Huang, Y., Zheng, R., Wei, S. Q., Ghirlando, R., Lee, M. S., Craigie, R., Gronenborn, A. M., and Clore, G. M. (1998) *Nature Struct. Biol.* **5**, 903-909
55. Clore, G. M., and Gronenborn, A. M. (1998) *Proc. Natl. Acad. Sci. U. S. A.* **95**, 5891-5898
56. Clore, G. M., Gronenborn, A. M., Nilges, M., and Ryan, C. A. (1987) *Biochemistry* **26**, 8012-8023
57. Nilges, M. (1993) *Proteins* **17**, 297-309
58. Shen, Y., Delaglio, F., Cornilescu, G., and Bax, A. (2009) *J. Biomol. NMR* **44**, 213-223
59. Schwieters, C. D., and Clore, G. M. (2001) *J. Magn. Reson.* **152**, 288-302
60. Schwieters, C. D., Kuszewski, J., and Clore, G. M. (2006) *Progr. NMR Spect.* **48**, 47-62
61. Schwieters, C. D., Kuszewski, J. J., Tjandra, N., and Clore, G. M. (2003) *J. Magn. Reson.* **160**, 65-73
62. Clore, G. M., Gronenborn, A. M., and Tjandra, N. (1998) *J. Magn. Reson.* **131**, 159-162
63. Kuszewski, J., Qin, J., Gronenborn, A. M., and Clore, G. M. (1995) *J. Magn. Reson. B* **106**, 92-96
64. Nilges, M., Gronenborn, A. M., Brunger, A. T., and Clore, G. M. (1988) *Protein Eng.* **2**, 27-38
65. Clore, G. M., and Kuszewski, J. (2002) *J. Am. Chem. Soc.* **124**, 2866-2867
66. Schwieters, C. D., and Clore, G. M. (2008) *J. Phys. Chem. B* **112**, 6070-6073
67. Schwieters, C. D., and Clore, G. M. (2001) *J. Magn. Reson.* **149**, 239-244
68. Nicholls, A., Sharp, K. A., and Honig, B. (1991) *Proteins* **11**, 281-296
69. Schwieters, C. D., and Clore, G. M. (2002) *J. Biomol. NMR* **23**, 221-225
70. Clore, G. M. (2000) *Proc. Natl. Acad. Sci. U. S. A.* **97**, 9021-9025

71. Clore, G. M., and Garrett, D. S. (1999) *J. Am. Chem. Soc.* **121**, 9008-9012
72. Bax, A., Kontaxis, G., and Tjandra, N. (2001) *Methods Enzymol.* **339**, 127-174
73. Williams, D. C., Jr., Cai, M., and Clore, G. M. (2004) *J. Biol. Chem.* **279**, 1449-1457
74. Williams, D. C., Jr., Lee, J. Y., Cai, M., Bewley, C. A., and Clore, G. M. (2005) *J. Biol. Chem.* **280**, 29269-29276
75. Ortega-Roldan, J. L., Jensen, M. R., Brutscher, B., Azuaga, A. I., Blackledge, M., and van Nuland, N. A. (2009) *Nucleic Acids Res.* **37**, e70
76. Jones, S., and Thornton, J. M. (1996) *Proc. Natl. Acad. Sci. U. S. A.* **93**, 13-20
77. Reynolds, C., Damerell, D., and Jones, S. (2009) *Bioinformatics* **25**, 413-414
78. Grzesiek, S., Stahl, S. J., Wingfield, P. T., and Bax, A. (1996) *Biochemistry* **35**, 10256-10261
79. Jones, T. A., Zou, J. Y., Cowan, S. W., and Kjeldgaard, M. (1991) *Acta Crystallogr. A* **47** 110-119
80. Sass, H. J., Musco, G., Stahl, S. J., Wingfield, P. T., and Grzesiek, S. (2001) *J. Biomol. NMR* **21**, 275-280
81. Laskowski, R. A., McArthur, M. W., Moss, D. S., and Thornton, J. M. (1993) *J. Appl. Crystallogr.* **26**, 283-291

FOOTNOTES

*This work was supported by the intramural program of NIDDK, NIH and the Intramural AIDS Targeted Antiviral Program of the Office of the Director of the National Institutes of Health (to G.M.C.).

The atomic coordinates and NMR experimental restraints (accession codes 2WWV for the unphosphorylated complex and 2WY2 for the phosphoryl transition state complex) have been deposited in the Protein Data Bank, Research Collaboratory for Structural Bioinformatics, Rutgers University, New Brunswick, NJ (<http://www.rcsb.org/>)

† These authors contributed equally to the work in this paper.

‡To whom correspondence should be addressed: Laboratory of Chemical Physics, Building 5, Rm B1-30I, NIDDK, National Institutes of Health, Bethesda, MD 20892-0520. Tel: 301-496-0782; Fax: 301-496-0825; E-mail: mariusc@mail.nih.gov.

¹The abbreviations used are: PTS, phosphoenolpyruvate:sugar phosphotransferase system; enzyme I, EI; HPr, histidine-containing phosphocarrier protein; Chb, N,N'-diacetylchitobiose; IIA^{Chb}, IIB^{Chb} and IIC^{Chb}, A, B and C domains, respectively, of the N,N'-diacetylchitobiose transporter II^{Chb}; IIA^{Chb*}, double mutant of IIA^{Chb} comprising a 13-residue deletion at the N-terminus and an Asp to Leu mutation at position 92 (wild type numbering). NOE, nuclear Overhauser effect; HSQC, heteronuclear single quantum coherence; TROSY, transverse relaxation optimized spectroscopy; rms, root mean square; RDC, residual dipolar coupling; AA, amino acid; ppb, parts per billion.

Figure legends

Fig. 1. Binding of IIA^{Chb*}(H89E) and IIB^{Chb}(C10S). Backbone amide chemical shift perturbations upon titrating unlabeled IIA^{Chb*}(H89E) into a solution of ¹⁵N-labeled IIB^{Chb}(C10S) at 20°C. The chemical shifts were monitored using ¹H-¹⁵N HSQC spectroscopy at a spectrometer ¹H frequency of 600 MHz. $\Delta\delta_{H/N} = [(\Delta\delta^{15N})^2/25 + (\Delta\delta^1H)^2/2]^{1/2}$ (78). The IIA^{Chb*}(H89E):IIB^{Chb}(C10S) molar ratios, expressed in terms of subunit concentration of IIA^{Chb*}(H89E), are 0, 0.2, 0.4, 1.0, 1.5 and 2.0, with corresponding subunit concentrations of IIA^{Chb*}(H89E) of 0, 0.10, 0.20, 0.47, 0.68 and 0.88 mM, respectively, and concentrations of IIB^{Chb}(C10S) of 0.5, 0.49, 0.49, 0.47, 0.45, 0.44 mM, respectively. The solid lines represent the results of a global non-linear least squares best-fit to all the titration data simultaneously, using a simple equilibrium binding model. The optimized K_D value is 1.3 ± 0.3 mM.

Fig. 2. Intermolecular NOEs in the IIA^{Chb*}(H89E)-IIB^{Chb}(C10S) complex. NOEs in a 3D ¹²C-filtered/¹³C-separated NOE experiment recorded in D₂O are specifically observed from protons attached to ¹²C (in the F₁ dimension) to protons attached to ¹³C (in the F₃ dimension). Strips are shown for NOEs involving the ¹³Cδ methyl groups of Ile72 and Ile26 of IIA^{Chb*}(H89E). The amino-acid specific labeling scheme used for [¹H-AA]/[²H, ¹²C, ¹⁴N]-IIB^{Chb}(C10S) is shown above each strip.

Fig. 3. Solution structure of the IIA^{Chb*}(H89E)-IIB^{Chb}(C10S) complex. A, Stereoview of a superposition of the backbone (N, Cα, C) atoms of the final 90 simulated annealing structures with the A, B and C subunits of the IIA^{Chb*}(H89E) symmetric trimer in *blue*, *gold* and *green*, respectively, and IIB^{Chb}(C10S) in *red*. The active site residues, H89E and C10S are shown in *purple* and *cyan*, respectively, and the *pink* meshes represent the atomic density probability map (69) for these two residues (drawn at a value of 20% maximum). Only a single IIB^{Chb} molecule binding at the interface of the A and C subunits of IIA^{Chb*}(H89E) is shown; since IIA^{Chb*}(H89E) is a symmetric trimer there are three identical binding sites formed at the interfaces between the A and C subunit, the C and B subunits and the B and A subunits. (B) Ribbon diagram of the complex showing two IIB^{Chb}(C10S) molecules bound to the IIA^{Chb*}(H89E) trimer. (C) Ribbon diagram of the complex with a view orthogonal to that shown in (B) depicting three molecules of IIB^{Chb}(C10S) bound to the IIA^{Chb*}(H89E) trimer. The color coding in (B) and (C) is the same as that in (A). D, Stereoview showing a reweighted atomic probability density map (drawn at a value of 20% maximum and calculated from the final 90 simulated annealing structures) for some of the interfacial side chains displayed as *purple* and *green* meshes for IIB^{Chb}(C10S) and the C chain of IIA^{Chb*}(H89E), respectively. The backbones are shown as tubes color coded as in (A); the sidechains of the restrained regularized mean structure are color coded according to atom type (carbon, *gray*; oxygen, *red*; and nitrogen, *blue*). Residues of IIB^{Chb}(C10S) are labeled in *italics*.

Fig. 4. The IIA^{Chb*}(H89E)-IIB^{Chb}(C10S) interface. A, Stereoview of the interface between the A subunit of IIA^{Chb*}(H89E) and IIB^{Chb}(C10S) with the respective backbones shown as transparent *blue* and *red* ribbons, respectively. B, Stereoview of the interface between the C subunit of IIA^{Chb*}(H89E) and IIB^{Chb}(C10S) with the respective backbones shown as transparent *green* and *red* ribbons, respectively. The dashed lines indicate intermolecular hydrogen bonds or salt bridges. The sidechain atoms are colored according to atom type; carbon, *gray*; nitrogen, *blue*; oxygen, *red*. Residues of IIB^{Chb}(C10S) are labeled in *italics*. C, Diagrammatic representation of the intermolecular contacts between the A and C subunits of IIA^{Chb*}(H89E) and IIB^{Chb}(C10S). Residues involved in sidechain-sidechain electrostatic interactions are colored in *blue* (donor) or *red* (acceptor). Ile72 of the C subunit of IIA^{Chb*}(H89E) is colored in *orange* since its backbone carbonyl accepts a hydrogen bond from Ser17 of IIB^{Chb}(C10S). The active site residues, H89E of IIA^{Chb*}(H89E), and C10S of IIB^{Chb}(C10S) are colored *purple*.

Fig. 5. Interaction surfaces for the IIA^{Chb*}(H89E)-IIB^{Chb}(C10S) complex. The left panel display the interaction surface (formed by the A and C subunits) on IIA^{Chb*}(H89E) for IIB^{Chb}(C10S); the right panel shows the interaction surface on IIB^{Chb}(C10S) for IIA^{Chb*}(H89E). The surfaces are color coded as follows: hydrophobic residues, *green*; uncharged residues bearing a polar functional group, *cyan*; negatively charged residues, *red*; positively charged residues, *blue*. Relevant portions of the backbone and active site residue of the interacting partner are displayed as tubes and bonds, respectively. Residues of IIB^{Chb}(C10S) are labeled in *italics*. Residues from the C subunit of IIB^{Chb}(H89E) are indicated by an apostrophe after the residue number;

in addition, the surfaces of the A and C subunits of $\text{IIA}^{\text{Chb}*}$ that do not constitute the interaction surface are colored in *dark gray* and *light gray*, respectively.

Fig. 6. The phosphoryl transition state of the $\text{IIA}^{\text{Chb}*}$ - IIB^{Chb} complex. A, Stereoview displaying the conformational change within the active site loop of IIB^{Chb} accompanying formation of a phosphoryl transition state. Superposition of the active site loop of the $\text{IIA}^{\text{Chb}*}$ - $\text{P-IIB}^{\text{Chb}}$ transition state (*solid colors*) and the $\text{IIA}^{\text{Chb}*}$ (H89E)- IIB^{Chb} (C10S) complex (*transparent colors*) with the backbones of $\text{IIA}^{\text{Chb}*}$ and IIB^{Chb} in *red* and *blue*, respectively (see text for further details). B, Stereoview of the environment surrounding the His89-P-Cys10 transition state. The backbone is displayed as transparent tubes with IIB^{Chb} in *red*, and the A and C subunits of $\text{IIA}^{\text{Chb}*}$ in *blue* and *green*, respectively. C, Schematic of the interactions stabilizing the transition state. The thick dashed lines indicate hydrogen bonds, the thin dashed lines indicate electrostatic interactions that are too long to be classified as hydrogen bonds. It should be noted that only sidechain torsion angle changes confined within a single rotamer would be required to permit hydrogen bonding interactions from His93^A (Chain A) and Gln91^C (Chain C) of $\text{IIA}^{\text{Chb}*}$ to the phosphoryl group in phopho- $\text{IIA}^{\text{Chb}*}$. Color coding: *red*, IIB^{Chb} ; *blue*, A subunit of $\text{IIA}^{\text{Chb}*}$; *green*, C subunit of $\text{IIA}^{\text{Chb}*}$. Residues of IIB^{Chb} are labeled in *italics*.

Fig. 7 Comparison of the $\text{IIA}^{\text{Chb}*}$ - IIB^{Chb} and IIA^{Mtl} - IIB^{Mtl} complexes. A, Overall stereoview and, B, stereo close up of the His-P-Cys phosphoryl transition state, with IIB^{Chb} and IIB^{Mtl} superimposed. The backbone is displayed as a ribbon diagram and the His-P-Cys transition state as a stick diagram. IIA^{Mtl} and IIB^{Mtl} are shown in *green* and *grey*, respectively; $\text{IIA}^{\text{Chb}*}$ and IIB^{Chb} are shown in *transparent blue* and *red*, respectively; and the His-P-Cys phosphoryl transition state is shown in *gold* for the $\text{IIA}^{\text{Chb}*}$ - IIB^{Chb} complex and in *purple* for the IIA^{Mtl} - IIB^{Mtl} complex. The coordinates of the IIA^{Mtl} - IIB^{Mtl} complex are taken from (36) (PDB code 2FEW). The superposition of IIB^{Chb} and IIB^{Mtl} was carried out using the program O (79).

Table 1

Labeling schemes for samples used for intermolecular NOE measurements on the IIA^{Chb}(H89E)-IIB^{Chb}(C10S) complex*

Sample	Isotope labeling	
	IIA ^{Chb*} (H89E)	IIB ^{Chb} (C10S)
1	[¹³ CH ₃ -ILV]/[² H/ ¹³ C/ ¹⁵ N]	[¹ H-Gly,Ser]/[² H/ ¹² C/ ¹⁴ N]
2	[¹³ CH ₃ -ILV]/[² H/ ¹³ C/ ¹⁵ N]	[¹ H-Pro,Tyr]/[² H/ ¹² C/ ¹⁴ N]
3	[¹³ CH ₃ -ILV]/[² H/ ¹³ C/ ¹⁵ N]	[¹ H-Met]/[² H/ ¹² C/ ¹⁴ N]
4	[¹ H-Thr]/[² H/ ¹² C/ ¹⁴ N]	U-[¹ H/ ¹³ C/ ¹⁵ N]
5	[¹ H-Met]/[² H/ ¹² C/ ¹⁴ N]	U-[¹ H/ ¹³ C/ ¹⁵ N]
6	[¹ H-Met]/[² H/ ¹² C/ ¹⁴ N]	[¹³ CH ₃ -ILV]/[² H/ ¹³ C/ ¹⁵ N]
7	[¹ H-Ile]/[² H/ ¹² C/ ¹⁴ N]	[¹³ CH ₃ -ILV]/[² H/ ¹³ C/ ¹⁵ N]
8	U-[¹ H/ ¹³ C/ ¹⁵ N]	[¹³ CH ₃ -ILV]/[² H/ ¹² C/ ¹⁴ N]
9	U-[¹ H/ ¹³ C/ ¹⁵ N]	[¹ H-Met,Tyr]/[² H/ ¹² C/ ¹⁴ N]

Table 2
RDC R-factors for IIB^{Chb}

	RDC R-factor (%) ^a		
	X-ray IIB ^{Chb} (C10S) ^b	NMR IIB ^{Chb} (C10S) ^b	NMR phospho-IIB ^{Chb} ^b
A. ¹D_{NH} RDCs measured on free IIB^{Chb}(C10S)^c			
100 mM NaCl and 10 mg/ml pf1			
all data (73) / excluding residues 9-16 (67)	12.1 / 8.0	44.7 / 43.8	18.8 / 14.4
active site loop (residues 9-16) (6) ^d	70.1	79.5	88.2
400 mM NaCl and 17 mg/ml pf1			
all data (80) / excluding residues 9-16 (74)	14.7 / 8.4	40.2 / 34.8	16.2 / 11.5
active site loop (residues 9-16) (6) ^d	50.9	88.4	50.2
B. ¹D_{NH} RDCs measured on free phospho-IIB^{Chb}^c			
100 mM NaCl and 10 mg/ml pf1			
all data (66) / excluding residues 9-16 (59)	38.8 / 16.8	55.4 / 49.3	19.9 / 20.8
active site loop (residues 9-16) (7) ^e	73.2	70.0	15.5
200 mM NaCl and 15 mg/ml pf1			
all data (76) / excluding residues 9-16 (69)	34.1 / 16.0	52.2 / 46.6	16.6 / 16.8
active site loop (residues 9-16) (7) ^e	70.6	70.9	15.3

^aThe RDC R-factor is defined as $100 \times \{ \langle (D_{obs} - D_{calc})^2 \rangle / 2 \langle D_{obs}^2 \rangle \}^{1/2}$ (71), where D_{obs} are the observed RDCs, and D_{calc} are the calculated RDCs obtained by singular value decomposition against the coordinates of the indicated protein (72). The values for the magnitude of the principal component of the alignment tensor (D_a^{NH}) and the rhombicity (η) are as follows. For the RDCs measured on free IIB^{Chb}(C10S), the values are 25.6 Hz and 0.4, respectively, in 100 mM NaCl and 10 mg/ml pf1, and -8.9 Hz and 0.3, respectively, in 400 mM NaCl and 17 mg/ml phage pf1; the normalized scalar product between the alignment tensors (80) at the two salt concentrations is -0.1, indicating that the two alignment tensors are effectively independent of one another. For the RDCs measured on free phospho-IIB^{Chb}, the values are 21.2 Hz and 0.53, respectively in 100 mM NaCl and 10 mg/ml phage pf1, and -9.6 Hz and 0.64, respectively in 200 mM NaCl and 15 mg/ml phage pf1, with a normalized scalar product of 0.96 between the two alignment tensors.

^bThe PDB accession codes are 1IIB and 1E2B for the X-ray (9) and NMR (10) structures of IIB^{Chb}(C10S), respectively; and 1H9C for the NMR structure of phospho-IIB^{Chb} (11). The active site residue is located at position 10, and the active site loop comprises residues 9-16.

^cThe number of experimentally measured ¹D_{NH} RDCs is shown in parentheses.

^dRDCs were measured for residues 9, 10, 11, 12, 13 and 16. The cross-peaks for the backbone amide groups of Met14 and Ser15 were too broad to permit measurement of the ¹J_{NH} splitting in the alignment media.

^eRDCs were measured for residues 9, 10, 11, 12, 13, 14 and 16. The cross-peak for the backbone amide group of Ser15 was too broad to permit measurement of the ¹J_{NH} splitting in the alignment media.

Table 3*Structural statistics*

The notation of the NMR structures are as follows: <SA> are the final 90 simulated annealing structures, (SA)_r is the restrained regularized mean structure of the IIA^{Chb*}(H89E)-IIB^{Chb}(C10S) complex

	<SA>	(SA) _r
Number of experimental NMR restraints		
Intermolecular interproton distance restraints	40	
IIB ^{Chb} intramolecular interproton distance restraints ^a	78	
IIA ^{Chb*} torsion angle restraints	44	
IIB ^{Chb} torsion angle restraints	38	
¹ D _{NH} RDCs for IIB ^{Chb} (C10S) ^b	153	
¹³ Cα/ ¹³ Cβ chemical shift restraints for IIB ^{Chb} (C10S) ^c	15	
R.m.s. deviation from interproton distance restraints (Å) ^d	0.003±0.003	0
R.m.s. deviation from torsion angle restraints (°) ^d	0.35±0.03	0.32
R.m.s. deviation from ¹³ Cα/ ¹³ Cβ shift restraints (ppm)	0.60±0.03	0.59
Measures of structural quality ^e		
Intermolecular repulsion energy (kcal·mol ⁻¹)	3.8±1.4	10.7
Intermolecular Lennard-Jones energy (kcal·mol ⁻¹)	-29.6±6.3	-31.0
Coordinate precision of the complex (Å) ^f		
Backbone (N, Cα, C', O) atoms	0.32±0.11	
Interfacial sidechain heavy atoms ^g	0.90±0.07	

^aThe intramolecular NOE-derived interproton distance restraints relate only to interfacial sidechains and to the active site loop (residues 9-16) of IIB^{Chb}(C10S).

^bThe ¹D_{NH} RDCs were measured for free IIB^{Chb}(C10S) in two alignment media (10 mg/ml pf1 and 100 mM NaCl; and 17 mg/ml phage pf1 and 400 mM NaCl) (see Table 2). The active site loop (residues 9-16) is given complete torsional degrees of freedom, while the remainder of the backbone is treated as a rigid body comprising the X-ray coordinates of IIB^{Chb}(C10S) (pdb code 1IIB (9)); thus, the orientation of the alignment tensor is determined by the rigid portion of IIB^{Chb}(C10S), while the conformation of the active site loop is determined by the ¹D_{NH} RDCs within the loop. The RDC R-factors for the rigid portion of IIB^{Chb}(C10S) are given in Table 2, while those for the active site loop of the restrained regularized mean structure of the complex are provided in Table 4.

^cThe ¹³Cα and ¹³Cβ chemical shift restraints involve only the active site loop (residues 9-16) of IIB^{Chb}(C10S).

^dNone of the structures exhibit interproton distance violations >0.3 Å or torsion angle violations >5°.

^eThe intermolecular repulsion energy is given by the value of the quartic van der Waals repulsion term calculated with a force constant of 4 kcal·mol⁻¹·Å⁻⁴ and a van der Waals radius scale factor of 0.78. The intermolecular Lennard-Jones van der Waals interaction energy is calculated using the CHARMM19/20 parameters and is *not* included in the target function used to calculate the structures.

^fDefined as the average r.m.s. difference between the final 90 simulated annealing structures and the mean coordinates. The value quoted for the backbone (which excludes residues 75-84 of IIA^{Chb} which are disordered and have a coordinate precision of 1.9 Å) provides a measure of the precision with which the orientation and translation of the two proteins in the complex have been determined, and does not take into account the backbone accuracy of the NMR coordinates of IIA^{Chb*}(H89E) (26) and the X-ray coordinates of IIB^{Chb}(C10S) (9) used for conjoined rigid body/torsion angle dynamics docking. The accuracy of the restrained regularized mean coordinates of IIA^{Chb*}(H89E), excluding the loop residues 75-84 that were given backbone torsional degrees of freedom can be estimated from the coordinate precision (0.4 Å (26)) and the value of 8.7% for the cross-validated RDC R-factor for the NH bond vectors (this paper), which suggests a coordinate accuracy

comparable to a 1.5-2 Å resolution crystal structure (73,74). The accuracy of the X-ray coordinates of IIB^{Chb}(C10S) (excluding the active site loop that was given backbone torsional degrees of freedom) is likely to be around 0.3 Å judging from the crystallographic resolution (1.8 Å) and R-factor (18.7% and 24.1% for R_{free}) (9), as well as the RDC R-factors (this paper, Table 2). The backbone precision for the active site loop of IIB^{Chb}(C10S), obtained from the ensemble of simulated annealing structures, is 0.55 Å. The percentage of residues in the most favored region of the Ramachandran map (81) is 95% for both IIA^{Chb*}(H89E) and IIB^{Chb}(C10S).

^gThe sidechains of IIA^{Chb*}(H89E) given torsional degrees of freedom during simulated annealing are: residues 18, 19, 21, 22, 25, 26, 28, 29, 32-34, 36, 40, 41, 58, 59, 62, 65, 66, 69, 70, 72-74, 85-91, 93, 98, 101. (Note that a non-crystallographic symmetry restraint ensures that the conformation of equivalent residues for the three chains of IIA^{Chb*}(H89E) are identical.) The sidechains of IIB^{Chb}(C10S) given torsional degrees of freedom are: residues 9-12, 14-22, 24, 37, 39, 40, 41-43, 46, 47, 59, 60, 62, 63, 81, 82, 84, 86 and 87.

Table 4

RDC R-factors for IIB^{Chb} in the IIA^{Chb}(H89E)-IIB^{Chb}(C10S) complex and corresponding phosphoryl transition state*

	RDC R-factor (%) ^a	
	Complex	Transition state
A. ¹D_{NH} RDCs measured on free IIB^{Chb}(C10S)^b		
<i>100 mM NaCl and 10 mg/ml pfl</i>		
all data (73)	8.1	16.7
active site loop (residues 9-16) (6) ^c	7.8	105.4
<i>400 mM NaCl and 17 mg/ml pfl</i>		
all data (80)	9.8	13.1
active site loop (residues 9-16) (6) ^c	7.8	38.3
B. ¹D_{NH} RDCs measured on free phospho-IIB^{Chb}^b		
<i>100 mM NaCl and 10 mg/ml pfl</i>		
all data (66)	44.1	15.1
active site loop (residues 9-16) (7) ^d	86.9	2.8
<i>200 mM NaCl and 15 mg/ml pfl</i>		
all data (76)	35.7	14.7
active site loop (residues 9-16) (7) ^d	76.7	11.8

^aSee Table 2 footnote *a* for definition.

^bThe number of experimentally measured ¹D_{NH} RDCs is shown in parentheses.

^cRDCs were measured for residues 9, 10, 11, 12, 13 and 16 (see Table 2, footnote *d*).

^dRDCs were measured for residues 9, 10, 11, 12, 13, 14 and 16 (see Table 2, footnote *e*).

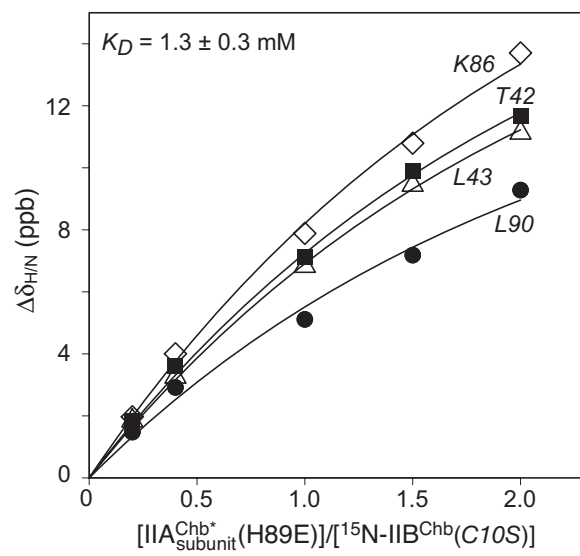


Fig. 1

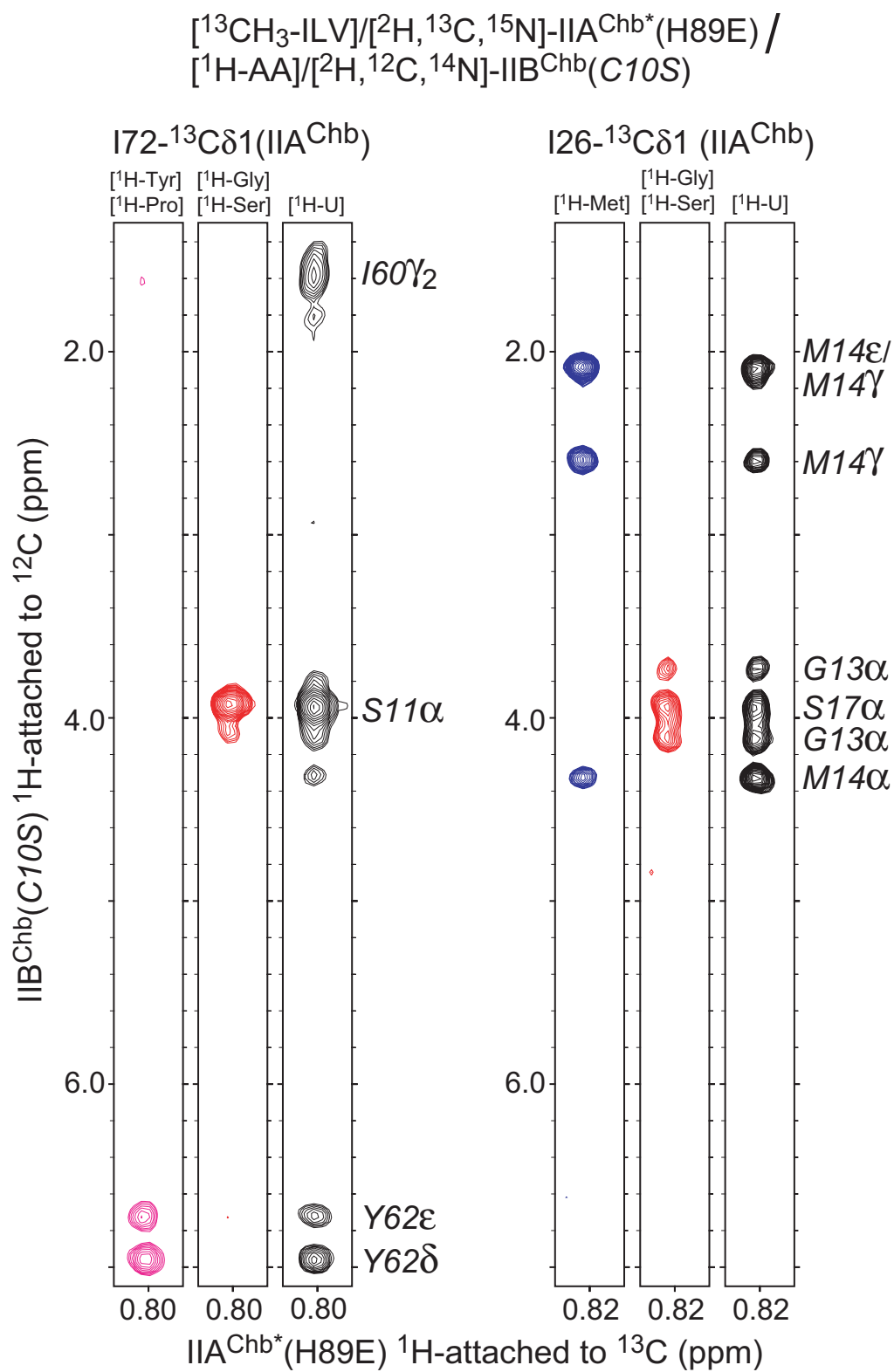


Fig. 2

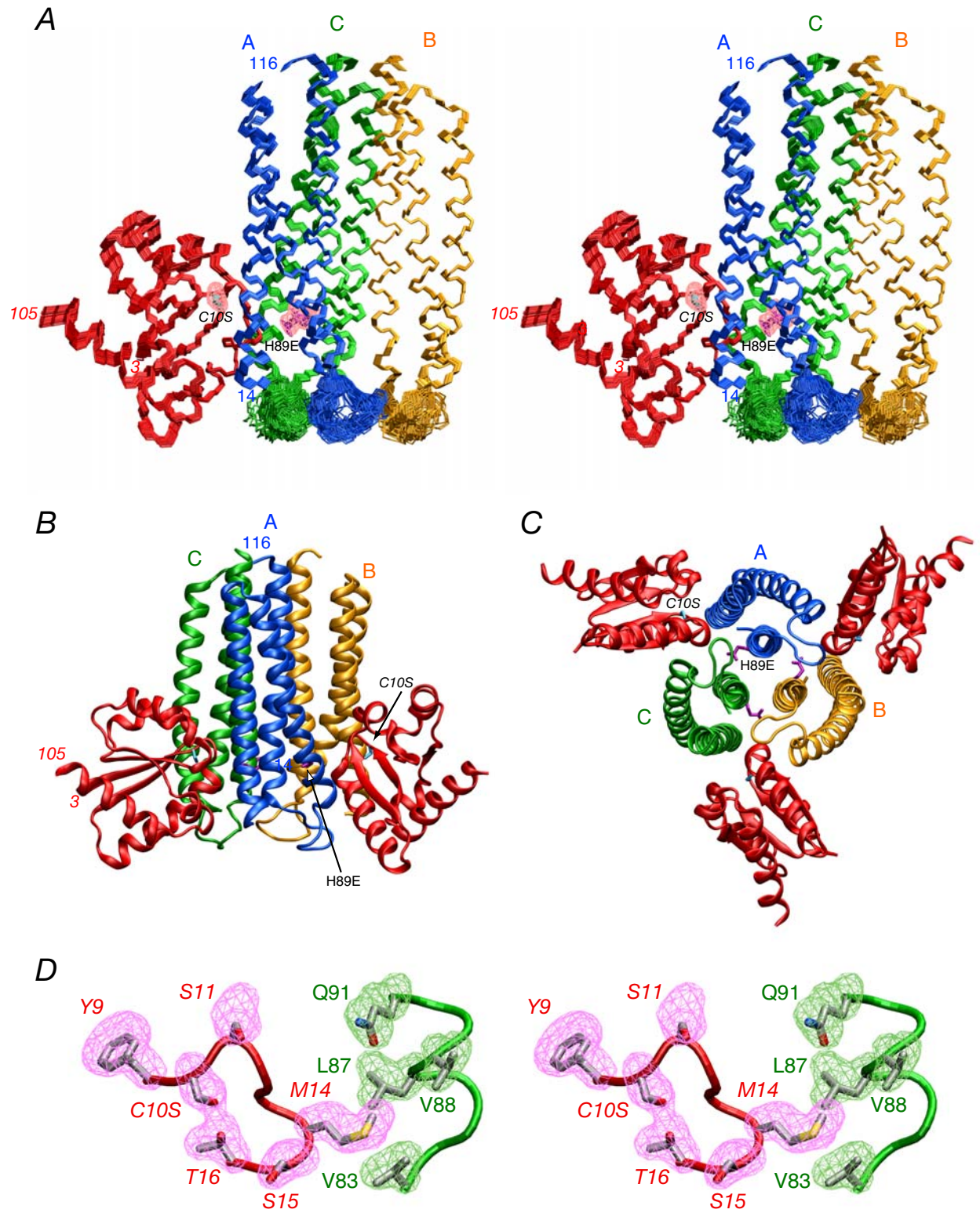


Fig. 3



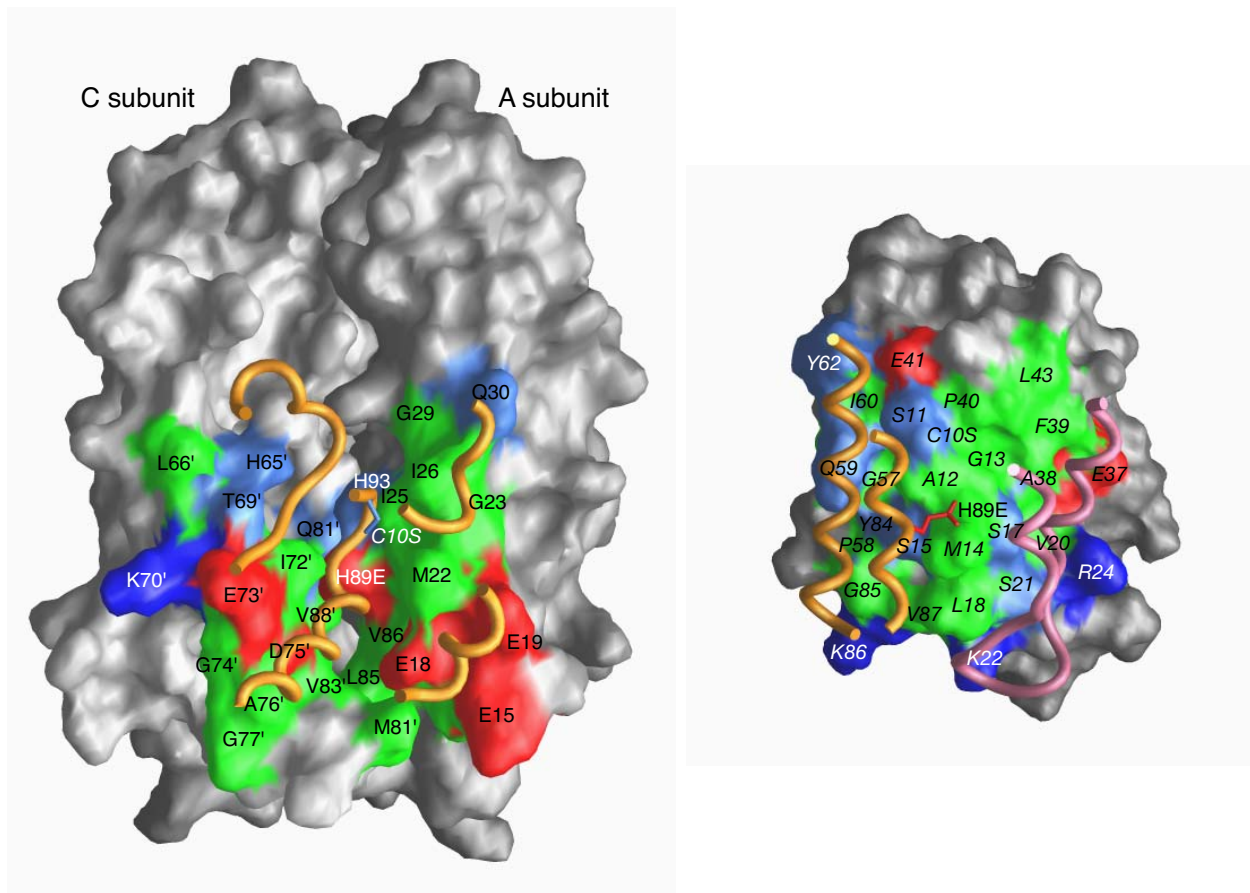


Fig. 5

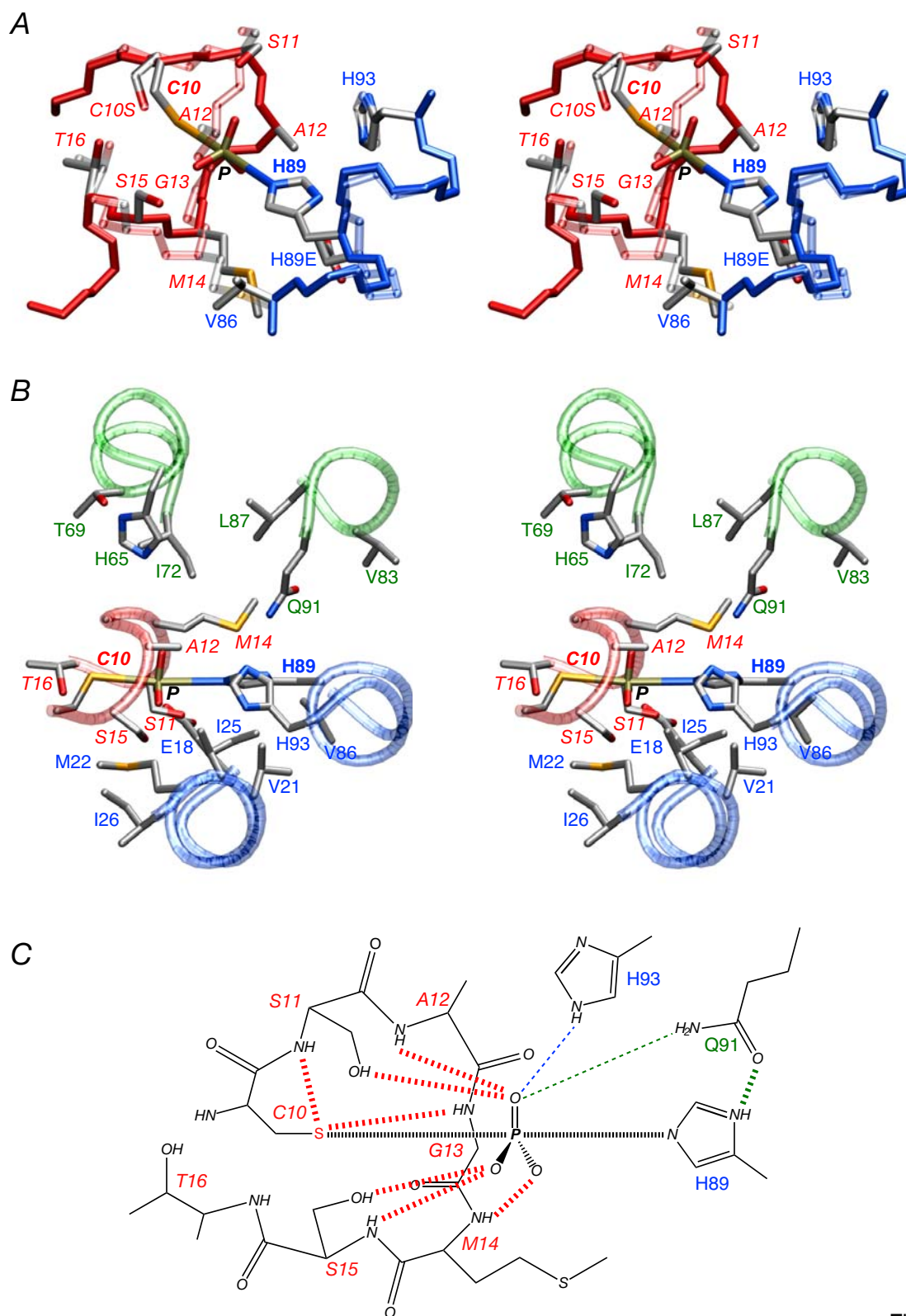


Fig. 6

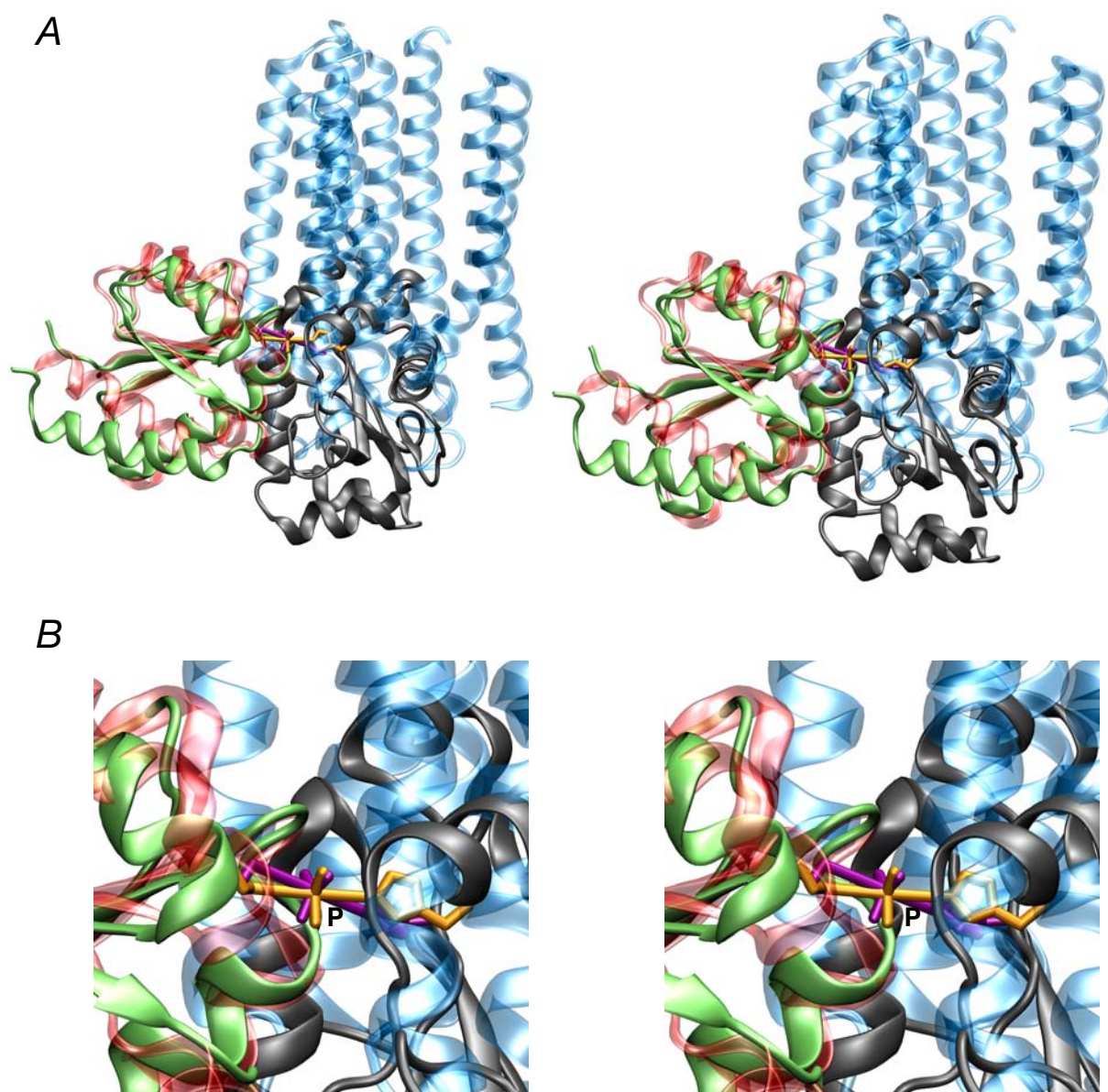


Fig. 7